JACS
JOURNAL OF THE AMERICAN CHEMICAL SOCIETY
pubs.acs.org/JACS
Article

Identification of the Highly Active Co−N_4 Coordination Motif for Selective Oxygen Reduction to Hydrogen Peroxide

Shanyong Chen,[#] Tao Luo,[#] Xiaoqing Li, Kejun Chen, Junwei Fu, Kang Liu, Chao Cai, Qiyou Wang, Hongmei Li, Yu Chen, Chao Ma, Li Zhu, Ying-Rui Lu, Ting-Shan Chan, Mingshan Zhu,* Emiliano Cortés,* and Min Liu*

Cite This: *J. Am. Chem. Soc.* 2022, 144, 14505−14516

Read Online

ACCESS | Metrics & More | Article Recommendations | Supporting Information

ABSTRACT: Electrosynthesis of hydrogen peroxide (H_2O_2) through oxygen reduction reaction (ORR) is an environment-friendly and sustainable route for obtaining a fundamental product in the chemical industry. Co−N_4 single-atom catalysts (SAC) have sparkled attention for being highly active in both 2e$^-$ ORR, leading to H_2O_2 and 4e$^-$ ORR, in which H_2O is the main product. However, there is still a lack of fundamental insights into the structure−function relationship between CoN_4 and the ORR mechanism over this family of catalysts. Here, by combining theoretical simulation and experiments, we unveil that pyrrole-type CoN_4 (Co−N SAC_{Dp}) is mainly responsible for the 2e$^-$ ORR, while pyridine-type CoN_4 catalyzes the 4e$^-$ ORR. Indeed, Co−N SAC_{Dp} exhibits a remarkable H_2O_2 selectivity of 94% and a superb H_2O_2 yield of 2032 mg for 90 h in a flow cell, outperforming most reported catalysts in acid media. Theoretical analysis and experimental investigations confirm that Co−N SAC_{Dp}—with weakening O_2/HOO* interaction—boosts the H_2O_2 production.

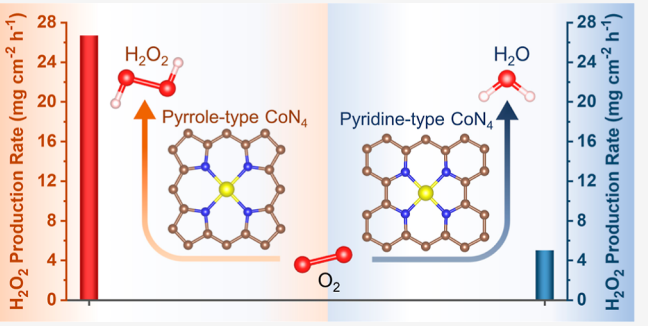

INTRODUCTION

Hydrogen peroxide (H_2O_2) is one of the most important chemicals, playing an essential role in chemical production, environmental treatment, paper and textile industry, and medical disinfection.[1−4] The demand for H_2O_2 is growing year by year, especially resulting from global public health safety troubles. The traditional industrial anthraquinone process for H_2O_2 production suffers from more and more serious challenges such as intensive energy consumption, large amounts of organic waste generation, and safety issues from the instability of H_2O_2 in transport and storage.[5−7] Recently, electroreduction of O_2 to H_2O_2 through a two-electron (2e$^-$) oxygen reduction reaction (ORR) has emerged as a promising alternative to the traditional anthraquinone process because of the environment-friendly merits and on-site production ability.[8−13] The key to realizing the electrosynthesis of H_2O_2 from 2e$^-$ ORR is to develop low-cost and high-performance catalysts. Currently, the development of high-performance 2e$^-$ ORR catalysts in alkaline systems has advanced satisfactorily.[14−20] However, the H_2O_2 production in acidic media possesses prominent advantages relative to the alkaline condition such as higher H_2O_2 stability (H_2O_2 in alkaline conditions is prone to self-decomposition). Most recently, the solid-state electrolytes were used to produce pure water−H_2O_2 solutions, which has gained special attention.[1,21,22] Nevertheless, the acidic H_2O_2 production is suitable for most actual application scenarios,[23,24] but state-of-the-art electrocatalysts for 2e$^-$ ORR in acid are presently lacking.

In recent years, there has been an incremental interest in searching for highly efficient and stable 2e$^-$ ORR catalysts in acid environments, including noble-based materials,[23,25−28] transitional metal compounds,[29−33] single-atom catalysts (SACs),[24,34−38] and carbon materials.[39−41] Among these, the carbon-based transition metal SAC has received special attention due to its high atom unitization, high electrical conductivity, and adjustable coordination environment.[37] For instance, both Liu *et al.*[42] and Strasser *et al.*[43] have screened different carbon-based transition metal SACs (such as Fe, Co, Ni, Cu, and Mn). They found that the Co SAC had the most 2e$^-$ ORR activity and the CoN_4 coordination structure was identified as the most active site. Recently, the Co SAC has emerged as the starred catalyst for 2e$^-$ ORR.[4,6,11,24,34] On the other hand, it is worth noting that the CoN_4 coordination structure has been demonstrated as the highly active site for 4e$^-$ ORR in quite a few previous studies.[44−49] For instance, Li

Received: January 30, 2022
Published: August 3, 2022

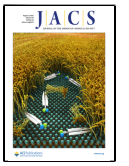

https://doi.org/10.1021/jacs.2c01194
J. Am. Chem. Soc. 2022, 144, 14505−14516

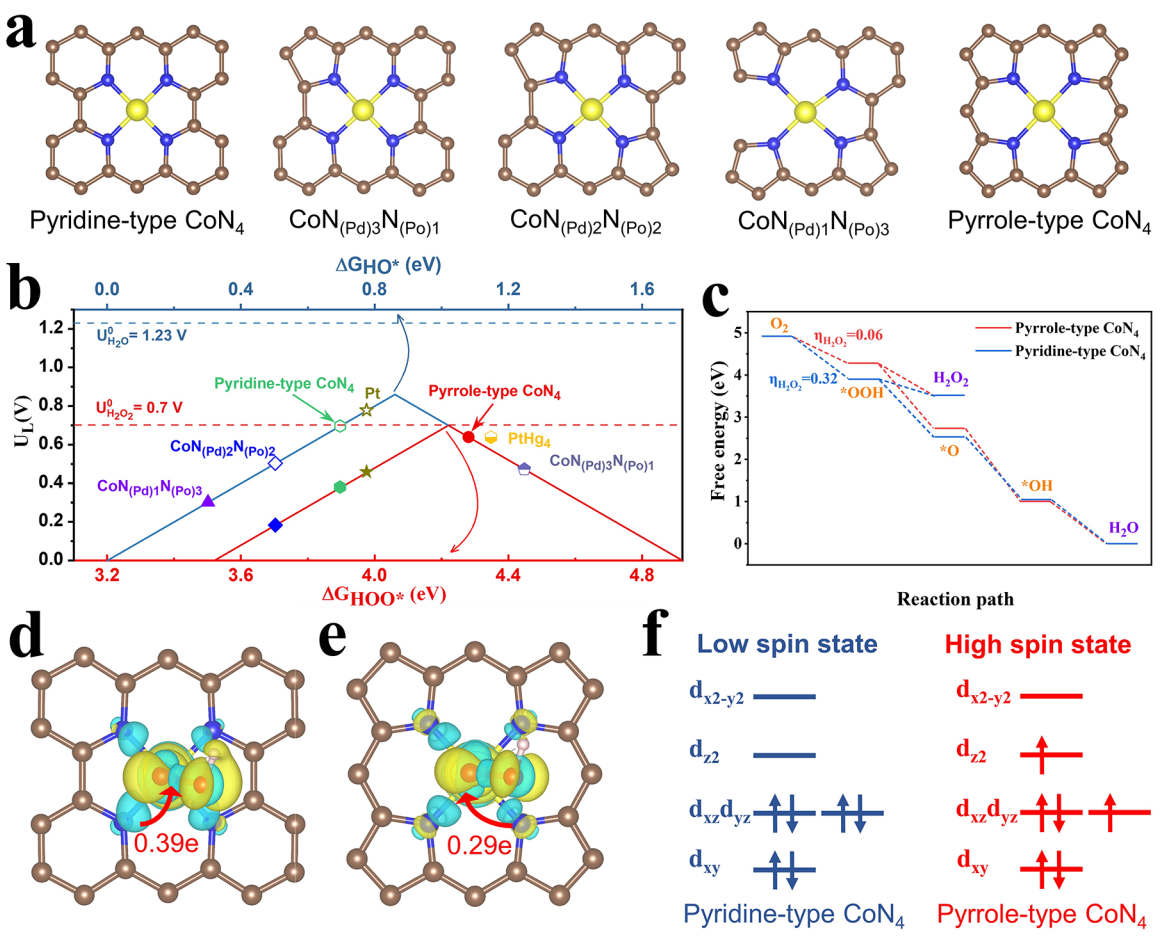

Figure 1. (a) Simulated different CoN_4 coordination structures. (b) Volcano plot depicting the Gibbs free energy of reaction intermediates (Δ_{HO*} and Δ_{HOO*}) on different Co−N coordination structures. The Pt and $PtHg_4$ were obtained from ref 25. (c) Free energy diagram of ORR on the pyridine-type and pyrrole-type CoN_4. (d) Differential charge distribution on pyridine-type CoN_4 with adsorption of HOO*. (e) Differential charge distribution on pyrrole-type CoN_4 with adsorption of HOO*. (f) 3d electron configuration of pyridine-type and pyrrole-type CoN_4 with adsorption of HOO*.

et al.[45] have prepared the single-atom CoN_4 in carbon matrix and demonstrated it as the outstanding $4e^-$ ORR catalyst with the high half potential of 0.773 V *versus* reversible hydrogen electrode (RHE) and low H_2O_2 selectivity of 0.76% at 0.8 V *versus* RHE in 0.5 M H_2SO_4. Summarizing present studies, the structure−function relationship between CoN_4 coordination structure and ORR pathway ($2e^-$ or $4e^-$ ORR) is highly controversial. The limited understanding is unfavorable for the development of high-performance catalysts for $2e^-$ ORR in the oxygen reduction community. Therefore, identification of the most active CoN_4 coordination structure for $2e^-$ ORR is greatly desirable, especially for the development of highly active and selective catalysts in acidic media.

Herein, we focus on the identification of the highly active CoN_4 coordination structure for $2e^-$ ORR among a series of prepared Co−N SAC to develop the high-performance catalyst for H_2O_2 production in acidic media. Theoretically, screened from a series of Co−N motifs, the pyrrole-type CoN_4 is found to show the optimal HOO* adsorption strength and highest $2e^-$ ORR activity. Experimentally, the three types of Co−N SACs (Co−N SAC_{Dp}, Co−N SAC_{Pc}, and Co−N SAC_{Mm}) are prepared using the pyrolysis strategy. Here, the Co−N SAC_{Dp} and Co−N SAC_{Mm} are obtained by using the nitrogen precursor of 4-dimethylaminopyridine and 2-methylimidazole, respectively, and the Co−N SAC_{Pc} involves in the pyrolysis of cobalt phthalocyanine (CoPc) during the synthesis process. The results of catalyst characterization and performance evaluation confirm that Co−N SAC_{Dp} (pyrrole-type CoN_4) formation occurs in the dominant $2e^-$ ORR pathway, while the Co−N SAC_{Mm} formation with pyridine-type CoN_4 occurs in the $4e^-$ ORR. Impressively, the Co−N SAC_{Dp} shows a remarkable mass activity of 14.4 A g_{cat}^{-1} (0.5 V *vs* RHE) and H_2O_2 selectivity of 94% in 0.1 M $HClO_4$. Furthermore, the Co−N SAC_{Dp} has been demonstrated to have a prominent H_2O_2 production rate of 26.7 mg cm^{-2} h^{-1} and H_2O_2 yield of up to 2032 mg for 90 h in the flow cell, leading to, for example, a practical electro-Fenton degradation of carbamazepine (CBZ). This work affords essential insights into the ORR mechanism based on SAC catalysts and the development of efficient catalysts for H_2O_2 production.

RESULTS AND DISCUSSION

Theoretical Calculation and ORR Mechanism. Among the most reported CoN_4 active sites,[3,42−45] the unsaturated pyridinic-N and pyrrolic-N are considered to be coordinated with the Co atom. Herein, we focus on varying the type of coordination nitrogen species in CoN_4 sites, which has less been investigated previously. A series of Co−N coordination structures with different amounts of pyridinic-N or pyrrolic-N are constructed (Figure 1a). Also, most models show a

https://doi.org/10.1021/jacs.2c01194
J. Am. Chem. Soc. 2022, 144, 14505−14516

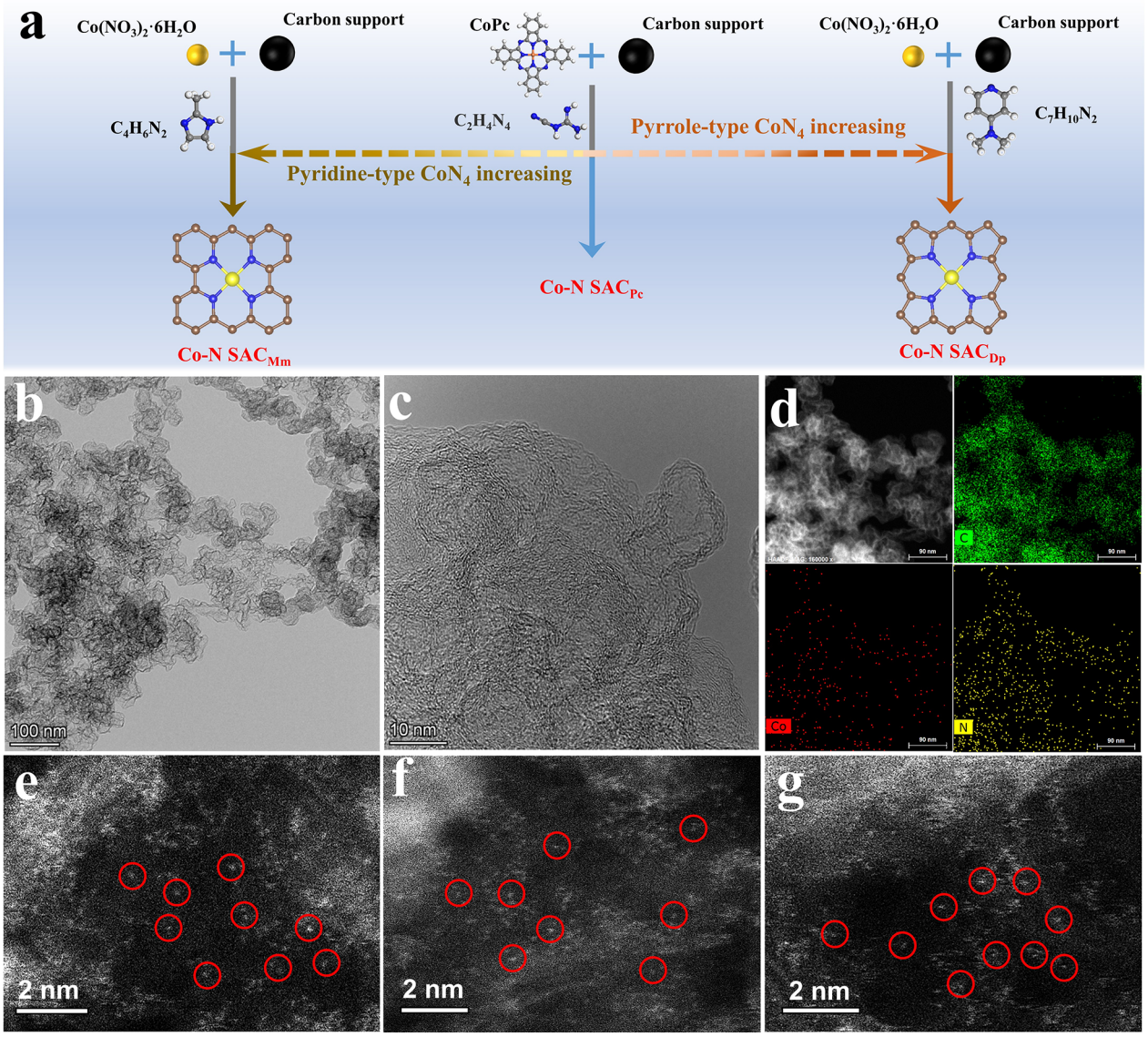

Figure 2. (a) Schematic diagram of the synthesis route for the three SAC catalysts. (b,c) TEM images, and (d) element mapping images of the Co−N SAC_{Dp}. AC-HAADF-STEM image of (e) Co−N SAC_{Dp}, (f) Co−N SAC_{Pc}, and (g) Co−N SAC_{Mm}.

thermodynamically favorable formation energy (Table S1). The pyridinic-N and pyrrolic-N are abbreviated as $N_{(Pd)}$ and $N_{(Po)}$, respectively. The HOO* and HO* are the crucial intermediates to determine if the reaction occurs through the $2e^-$ or $4e^-$ ORR pathway, and the Gibbs free energy of them (Δ_{HO*} and Δ_{HOO*}) for different Co−N coordination structures are computed. As shown in Figure 1b, Δ_{HO*} is related to $4e^-$ ORR, while Δ_{HOO*} governs H_2O_2 production through $2e^-$ ORR. According to the previous reports,[25,50] there is an approximately linear relationship between the Δ_{HO*} and Δ_{HOO*} with a constant value of 3.2 ± 0.2 eV. Besides, the strong adsorption of HOO* or HO* is located in the left region, and the weak adsorption corresponds to the right downhill in the volcano plot. The pyridine-type CoN_4, $CoN_{(Pd)1(Po)3}$, and $CoN_{(Pd)2(Po)2}$ with strong adsorption of HOO* prefer to break O−O bond, proceeding the $4e^-$ ORR pathway. More interestingly, the pyridine-type CoN_4 approaches the Pt implying the excellent $4e^-$ ORR activity. In sharp contrast, the pyrrole-type CoN_4 shows Δ_{HOO*} of 4.28 eV, which is close to the optimal HOO* adsorption energy of 4.22 eV (corresponding to limiting the potential of 0.7 V), meaning the main $2e^-$ ORR process. Impressively, the pyrrole-type CoN_4 exhibits better $2e^-$ ORR performances than other Co−N coordination structures, considering the small overpotential, which is comparable to the prominent $PtHg_4$ catalyst[25] (Figures 1b and S1). These results indicate that the coordination nitrogen type may govern the ORR pathway for CoN_4, and pyrrole-type CoN_4 is identified as the most active motif for H_2O_2 production. These results also can address the contradictory phenomenon that the CoN_4 sites are highly active for both $2e^-$ ORR and $4e^-$ ORR reported in previous reports.[42−49]

Next, we focus on the investigation of distinctly different ORR processes on the pyrrole-type CoN_4 and pyridine-type CoN_4. The general $2e^-$ and $4e^-$ ORR pathway can be depicted as follow (* indicates the catalytically-active site):

$$2e^- \text{ ORR pathway: } O_2 + 2(H^+ + e^-) \rightarrow H_2O_2 \quad U^0 = 0.70 \text{ V} \tag{1}$$

https://doi.org/10.1021/jacs.2c01194
J. Am. Chem. Soc. 2022, 144, 14505−14516

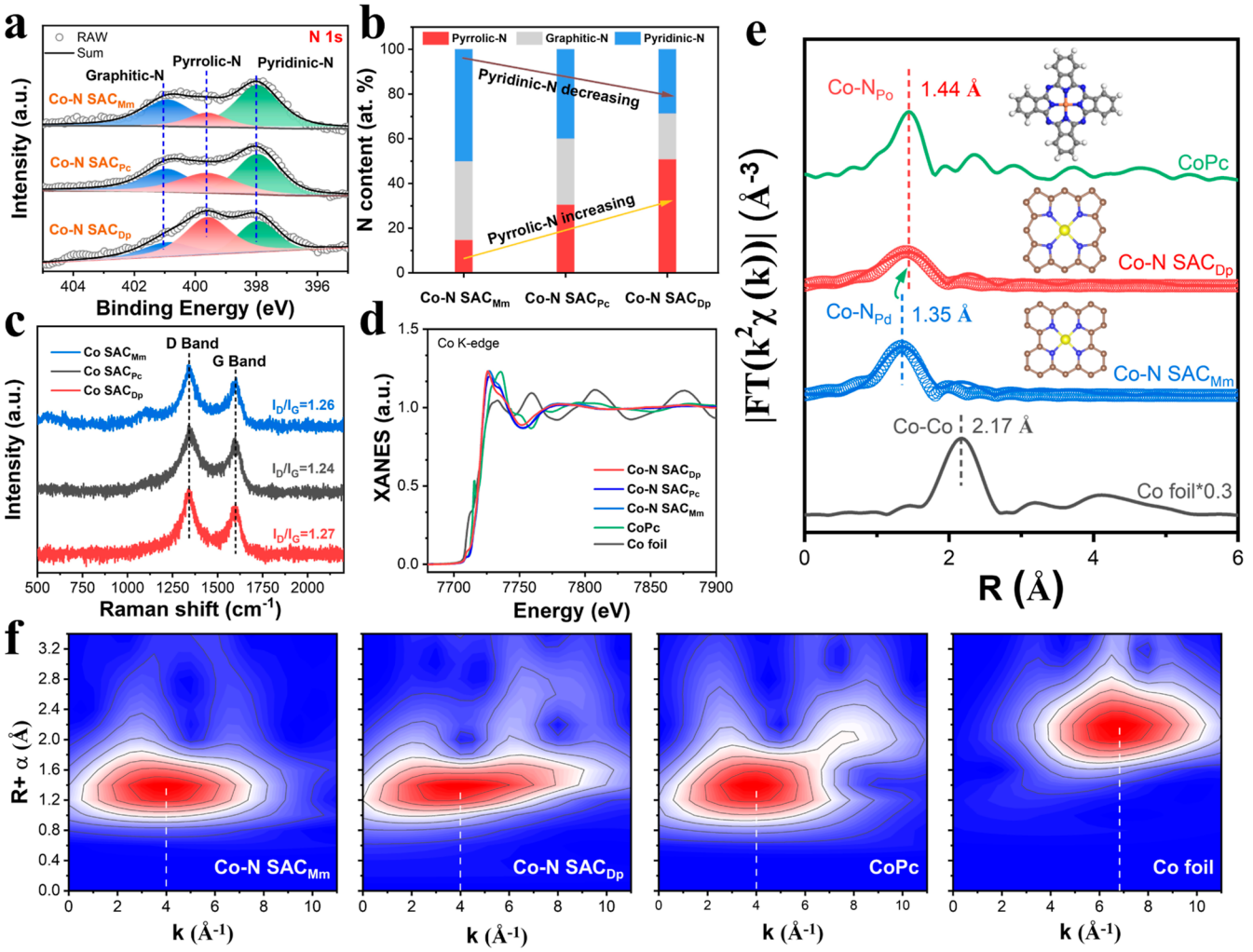

Figure 3. (a) N 1s XPS spectra, (b) proportion of different N species, and (c) Raman spectra of the three samples. (d) Co K-edge XANES spectra and (e) FT k_2-weighted and fitting extended XAFS (EXAFS) spectra of the Co−N SAC_{Dp}, Co−N SAC_{Mm}, and reference samples, inset: actual or fitting model. (f) Wavelet transform (WT) k^2-weighted EXAFS contour plots of the Co−N SAC_{Dp}, Co−N SAC_{Mm}, and the reference samples.

$$^* + O_2 + H^+ + e^- \rightarrow {}^*OOH \quad (1a)$$

$$^*OOH + H^+ + e^- \rightarrow H_2O_2 + {}^* \quad (1b)$$

$$4e^- \text{ ORR pathway: } O_2 + 4(H^+ + e^-) \rightarrow 2H_2O$$

$$U^0 = 1.23 \text{ V} \quad (2)$$

$$^* + O_2 + H^+ + e^- \rightarrow {}^*OOH \quad (2a)$$

$$^*OOH + H^+ + e^- \rightarrow H_2O + O^* \quad (2b)$$

$$O^* + H^+ + e^- \rightarrow OH^* \quad (2c)$$

$$OH^* + H^+ + e^- \rightarrow H_2O + {}^* \quad (2d)$$

For O_2 reduction to H_2O_2 through $2e^-$ ORR, the pyrrole-type CoN_4 shows a lower thermodynamic overpotential (η) of 0.06 eV (Figure 1c) relative to the pyridine-type CoN_4 ($\eta_{H_2O_2}$ = 0.32 eV). For $4e^-$ ORR to produce H_2O, the pyridine-type CoN_4 (η_{H_2O} = 0.21 eV) exhibits a smaller thermodynamic overpotential than that of pyrrole-type CoN_4 (η_{H_2O} = 0.59 eV). These results reveal that pyrrole-type CoN_4 prefers the $2e^-$ ORR (Figure S2), while the pyridine-type CoN_4 tends to proceed via $4e^-$ ORR (Figure S3), in accordance with the results from the volcano plot (Figure 1b). Importantly, the kinetic analyses also confirm the kinetic favorable HOO* protonation process rather than HOO* dissociation on pyrrole-type CoN_4 (Figure S4-5). Furthermore, we investigate the interplay between the CoN_4 sites and the important HOO* intermediate, which largely determines the ORR pathway. As shown in Figure 1d,e, the pyridine-type CoN_4 shows a more prominent electron transfer (0.39 e) from the CoN_4 site to HOO* intermediate as compared to the pyrrole-type CoN_4 (0.29 e) determined by Bader charge analysis. This result indicates the strong electron interaction between the pyridine-type CoN_4 and HOO*. Moreover, the density of states (DOS) of Co in pyrrole-type and pyridine-type CoN_4 with adsorption of HOO* were calculated (Figure S6), and the Co orbital occupation of electrons are shown in Figure 1f. After adsorption of HOO*, there are two single electrons in the $d_{yz}d_{xz}$ and d_{z^2} orbits for Co of pyrrole-type CoN_4, while the electrons are paired in Co of pyridine-type CoN_4. It is reported that the high spin state is associated to the weaker adsorption of the HOO* intermediate relative to the low spin state.[51,52] Therefore, after adsorption of HOO*, the pyrrole-type CoN_4 showing a high spin state facilitate the HOO* desorption to generate H_2O_2. However, the pyridine-type CoN_4 with the low

https://doi.org/10.1021/jacs.2c01194
J. Am. Chem. Soc. 2022, 144, 14505−14516

spin state tends to dissociate the O−O bond in HOO* and, lastly, form H_2O. These results elucidate that the different ORR pathways for pyrrole-type and pyridine-type CoN_4 may come from the electron interaction with the important reaction intermediate (such as HOO*) and the accompanying spin state difference.

Synthesis and Characterization of Co−N SAC. Inspired by the density functional theory (DFT) results, we prepared three different Co−N SACs through a pyrolysis strategy (synthesis details see the Experimental Section in Supporting Information). To exclude the effect of the carbon support, the Ketjen Black (ECP600JD) is used as the support for the three Co−N SACs (Figure 2a). Thereinto, the Co−N SAC_{Dp} represents the sample derived from the 4-dimethylaminopyridine and cobaltous nitrate hexahydrate. The Co−N SAC_{Pc} comes from pyrolysis of CoPc and dicyandiamide. For Co−N SAC_{Mm}, the 2-methylimidazole and cobaltous nitrate hexahydrate are employed as the nitrogen and Co sources, respectively. Herein, considering the different transformation processes of the nitrogen precursor and coordination strength with the Co[53,54] (Figure S7), altering the nitrogen precursor may result in a different coordination structure for Co−N SAC samples.

The structure and morphology of the catalysts are characterized by scanning electron microscopy (SEM), transmission electron microscopy (TEM), and aberration-corrected high-angle annular dark-field scanning TEM (AC-HAADF-STEM). As shown in Figure S8, the three Co−N SAC samples show a similar nanoparticle morphology for the initial carbon black. As shown in TEM images (Figures 2b,c, S9a,b, and S10a,b), there are only wrinkled carbon nanoparticles without obvious metal particles. The X-ray diffraction (XRD) patterns (Figure S11) show the only (002) peak for graphite carbon at about 26° and the absence of metal nanoparticles. The HAADF-TEM and element mapping images (Figures 2d, S9c−f, and S10c−f) reveal that the Co and nitrogen are homogeneously dispersed in the carbon matrix, indicating the atomical dispersion of Co for the three Co−N SAC samples. The AC-HAADF-STEM measurements are carried out to investigate the Co single-atom in the three samples. As displayed in Figure 2e−g, the bright and isolated metal atoms can be observed, confirming the successful preparation of the three Co−N SAC samples.

To ascertain the chemical state and coordination structure, the X-ray photoelectron spectroscopy (XPS) and X-ray absorption fine structure (XAFS) were performed. Deconvolution of N 1s XPS spectra (Figure 3a) confirms that all the three Co−N SAC samples contain the pyridinic-N (398.0 eV), pyrrolic-N (399.6 eV), and graphitic-N (400.9 eV) species.[55−57] However, the proportion of the three N species has a great difference (Figure 3b and Table S2), suggesting the different coordination environments. Previous studies demonstrated that the transition metals tended to coordinate with the N species to form the MN_4 structure, in which the pyridinic-N and pyrrolic-N species were generally considered.[3,43−45] In our prepared three Co−N SAC samples, the Co−N SAC_{Dp} shows the highest content of pyrrolic-N species (50.9%) while the Co−N SAC_{Mm} exhibits the highest content of pyridinic-N species (50.0%, Figure 3b, and Table S2). That is to say, the Co−N SAC_{Dp} may dominate the pyrrole-type CoN_4 sites while the Co−N SAC_{Mm} mainly contains the pyridine-type CoN_4 sites. The Fourier transform infrared (FT-IR) spectra (Figure S12) show that all the three Co−N SAC samples exhibit a peak at 803 cm^{-1} which is related to the Co−N bonds.[57] Especially, the Co−N SAC_{Dp} emerges the characteristic stretch peak of pyrrole-type metal−N at 853 cm^{-1}, which has been identified in Fe phthalocyanine and pyrrole-type FeN_4 in the previous reports.[57,58] According to the N K-edge X-ray absorption near edge structure (XANES) spectra (Figure S13), the more distinct pyrrolic-N species can be identified for the Co−N SAC_{Dp} relative to the Co−N SAC_{Mm}. Moreover, the splitting pyrrolic-N peak (pyrrolic-N′) for the Co−N SAC_{Dp} may be related to the metal−pyrrolic N site.[57] Although no oxygen-containing chemicals have been used in the preparation process, the oxygen signals have been detected in XPS for the three Co−N SACs and a similar phenomenon also has occurred in previously reported SAC materials.[42,43,46,48] All the three Co−N SAC samples show similar oxygen functional groups and contents (Figure S14 and Table S3), which is expected to have less impact on ORR performances.

It is shown in Co K-edge XANES spectra (Figure 3d) that the Co−N SAC_{Dp} and Co−N SAC_{Mm} exhibit higher pre-edge absorption energy than the Co foil but is comparable to the CoPc, indicating the positive valency of Co. The Fourier-transformed EXAFS spectra (Figure 3e) prove the absence of Co−Co bonds (2.17 Å) in the Co−N SAC_{Dp} and Co−N SAC_{Mm} further verifying the single-atom dispersion of Co, which agrees well with the AC-HAADF-STEM results. Moreover, the main peaks in 1.35 Å for the Co−N SAC_{Mm} and 1.44 Å for the Co−N SAC_{Dp} are ascribed to the Co−N coordination structure referring to the CoPc and the reported SACs.[35,42,45,48] Noting that the slightly shifted Co−N peak between the Co−N SAC_{Mm} and Co−N SAC_{Dp} may come from the different Co−N coordination structures. Interestingly, the position of the Co−N peak in the Co−N SAC_{Dp} is equivalent to that in CoPc, suggesting the Co−pyrrolic-N (Co−N_{Po}) coordination structure in the Co−N SAC_{Dp}.

Furthermore, the quantitative least-squares fitting of EXAFS spectra confirms (Figures 3e and S15, S16) that the Co atom is coordinated with four pyrrolic-N in the Co−N SAC_{Dp}, while the four coordinated nitrogen species are pyridinic-N for the Co−N SAC_{Mm} screened from different theoretical models (Figures S17, S18, Tables S4, and S5). Besides, the Co−N SAC_{Pc} matches well with the $CoN_{(Pd)3(Po)1}$ model where the Co atom is coordinated with three pyridinic-N and one pyrrolic-N (Figure S19). The coordination number for the Co−N SAC_{Dp} and Co−N SAC_{Mm} is 3.86 and 3.88 (Table S6), respectively. The bond length of Co−N_{Po} (2.02 Å) in the Co−N SAC_{Dp} is longer than that of Co−N_{Pd} (1.90 Å) in the Co−N SAC_{Mm}, which is also corroborated by the proposed DFT model (Figure S20). As shown in the WT-EXAFS contour plots (Figure 3f), the three samples (Co−N SAC_{Dp}, Co−N SAC_{Mm}, and CoPc) with the Co−N coordination structure exhibit an intensity maximum of about 4 $Å^{-1}$, which is different from the 6.8 $Å^{-1}$ of Co−Co bond in Co foil. Summarizing the abovementioned results, we have experimentally confirmed the pyridine-type CoN_4 (Co−N SAC_{Dp}) and pyrrole-type CoN_4 (Co−N SAC_{Mm}) as illustrated in DFT simulation.

The physicochemical property has been further studied by Brunauer−Emmett−Teller (BET) specific surface area and Raman spectroscopy. The three Co−N SAC samples show the typical mesopore structure (Figure S21) and a comparable BET-specific surface area (Table S7). The characteristic D band and G band can be observed (Figure 3c) for carbon-based materials. Also, the intensity ratio of I_D/I_G for the Co−N

https://doi.org/10.1021/jacs.2c01194
J. Am. Chem. Soc. 2022, 144, 14505−14516

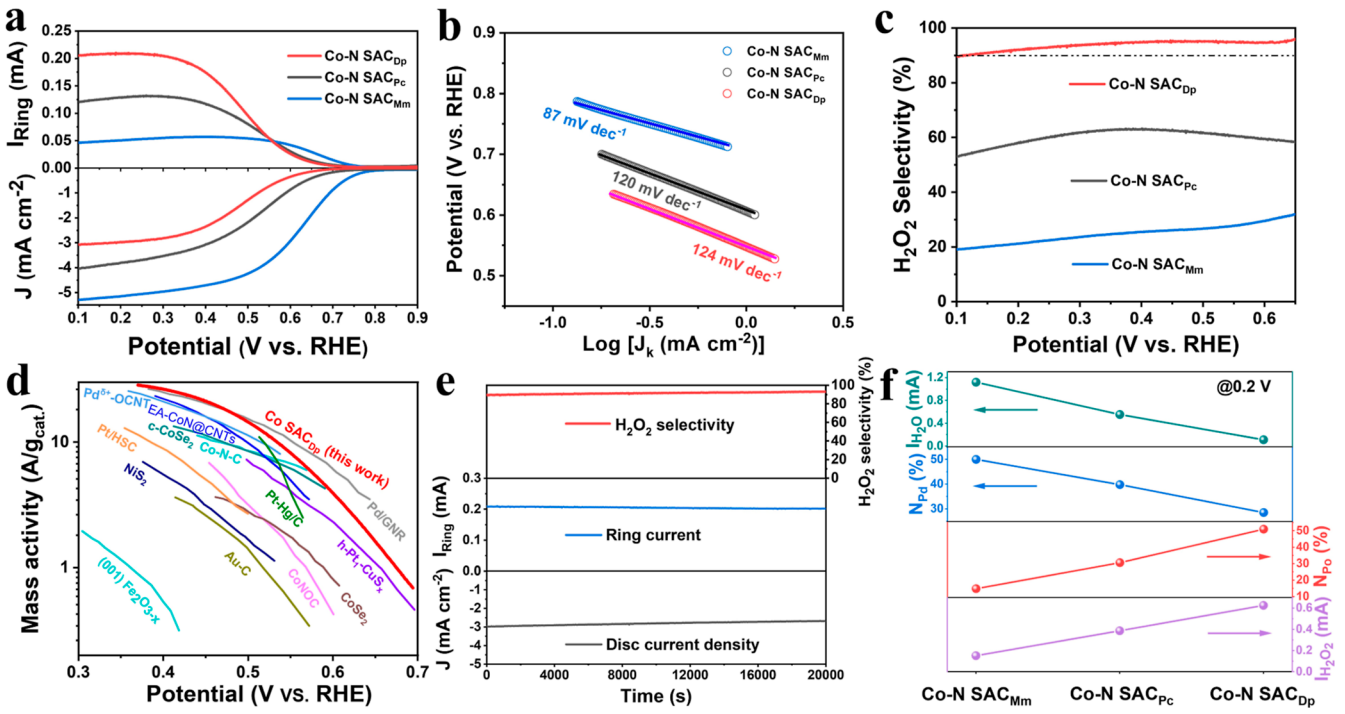

Figure 4. (a) ORR polarization curves of RRDE at 1600 rpm in 0.1 M $HClO_4$. (b) Calculated Tafel plots. (c) H_2O_2 selectivity. (d) Mass activity of the Co−N SAC_{Dp} and recently reported catalysts (the detailed information about these reference catalysts can see in Table S11). (e) Chronoamperometry measurement of the Co−N SAC_{Dp} for 20,000 s at 0.25 V (*vs* RHE). (f) Correlation between I_{H_2O} and $I_{H_2O_2}$ current at 0.2 V (*vs* RHE) and the proportion of nitrogen species for the three Co−N SACs.

SAC_{Dp}, Co−N SAC_{Pc}, and Co−N SAC_{Mm} is comparable, indicating a similar defect degree after N-doping. Thus, the three Co−N SAC samples can be used to study the structure−function relationship between the Co−N coordination structure and the ORR pathway, due to the similar physicochemical parameters and similar element contents (Table S8) but different local coordination structures.

ORR Performances and Experimental Investigation. Now, we turn to the investigation of ORR performances. The ORR measurement is performed on the three-electrode system with the rotating ring-disk electrode (RRDE) used as the working electrode. Prior to the ORR performance evaluation, the collection efficiency (N) of the RRDE has been determined (Figure S22). Also, the ORR polarization curves are collected on RRDE at 1600 rpm in O_2-saturated 0.1 M $HClO_4$. As shown in Figure 4a, the ORR activity follows the order: Co−N SAC_{Mm} > Co−N SAC_{Pc} > Co−N SAC_{Dp} in terms of the $E_{-0.2}$ (The potential corresponds to the current density of −0.2 mA cm^{-2}) and limiting current density (J_L). Thereinto, the Co−N SAC_{Mm} exhibits a high $E_{-0.2}$ of 0.767 V *versus* RHE (Table S9) and large J_L of 5.47 mA cm^{-2}, in correspondence with the reported typical 4e$^-$ ORR polarization curves.[45,46,48] Besides, the calculated electrochemical surface area (ECSA) based on the CV curves at different sweep rates accords well with the order of ORR activity (Figure S23 and Table S10). Using Koutecky−Levich (K−L) diffusion equation, the Tafel slopes of the Co−N SAC_{Mm}, Co−N SAC_{Pc}, and Co−N SAC_{Dp} are calculated to be 87, 120, and 124 mV dec^{-1} (Figure 4b), respectively, implying the different reaction kinetics and rate-determining step (RDS).[59,60] Thereinto, the RDS of Co−N SAC_{Mm} may relate to the HOO* dissociation,[20] while the first electron transfer process (* + O_2 + e$^-$ → *O_2^-) is ascribed to the RDS for the Co−N SAC_{Pc} and Co−N SAC_{Dp}.[37,42] The Co−N SAC_{Mm} and Co−N SAC_{Dp} show the transfer electron number (n) of 3.6−3.5 and 2.3−2.2 in the potential range of 0.6−0.2 V *versus* RHE, respectively, indicating the dominant 4e$^-$ ORR and 2e$^-$ ORR, respectively (Figure S24). Furthermore, according to the ORR polarization curves at different rotate rates and K−L diffusion equation, the n of the Co−N SAC_{Mm} and Co−N SAC_{Dp} is determined to be 3.7 and 2.2 (Figures S25 and S26), respectively. This result is consistent with the RRDE results. To investigate the relationship between the coordination structure and ORR pathway, the correlation between the content of nitrogen species and I_{H_2O} and $I_{H_2O_2}$ (0.2 V *vs* RHE) is concluded in Figure 4f. The $I_{H_2O_2}$ increases with the incremental content of pyrrolic-N (N_{Po}), while the I_{H_2O} decreases with the reduced content of pyridinic-N (N_{Pd}). Also, this result implies that pyrrole-type CoN_4 (Co−N SAC_{Dp}) contributes to 2e$^-$ ORR for H_2O_2 generation, while the pyridine-type CoN_4 (Co−N SAC_{Mm}) accounts for the 4e$^-$ ORR to form H_2O through an associative mechanism.[37] These analyses from catalytic performances agree well with the DFT calculation results.

Considering the dominant 2e$^-$ ORR pathway on the Co−N SAC_{Dp}, we focus on its performance for H_2O_2 production. Screened from the pyrolysis temperature of 700 to 900 °C (Figure S27), the Co−N SAC_{Dp} pyrolyzed at 800 °C is found to show the highest 2e$^-$ ORR performance. The optimal Co−N SAC_{Dp} exhibits a remarkable H_2O_2 selectivity of 94% at 0.3 V *versus* RHE (Figure 4c), outperforming that of the Co−N SAC_{Pc} (62%) and Co−N SAC_{Mm} (23%). Impressively, the Co−N SAC_{Dp} reveals a superior mass activity of 14.4 A $g_{cat.}^{-1}$ (0.5 V *vs* RHE), prominent Co mass activity (Figure S28), and a wide potential range (0.65−0.1 V *vs* RHE) of >90% selectivity for H_2O_2 production. The 2e$^-$ ORR of the Co−N

https://doi.org/10.1021/jacs.2c01194
J. Am. Chem. Soc. 2022, 144, 14505−14516

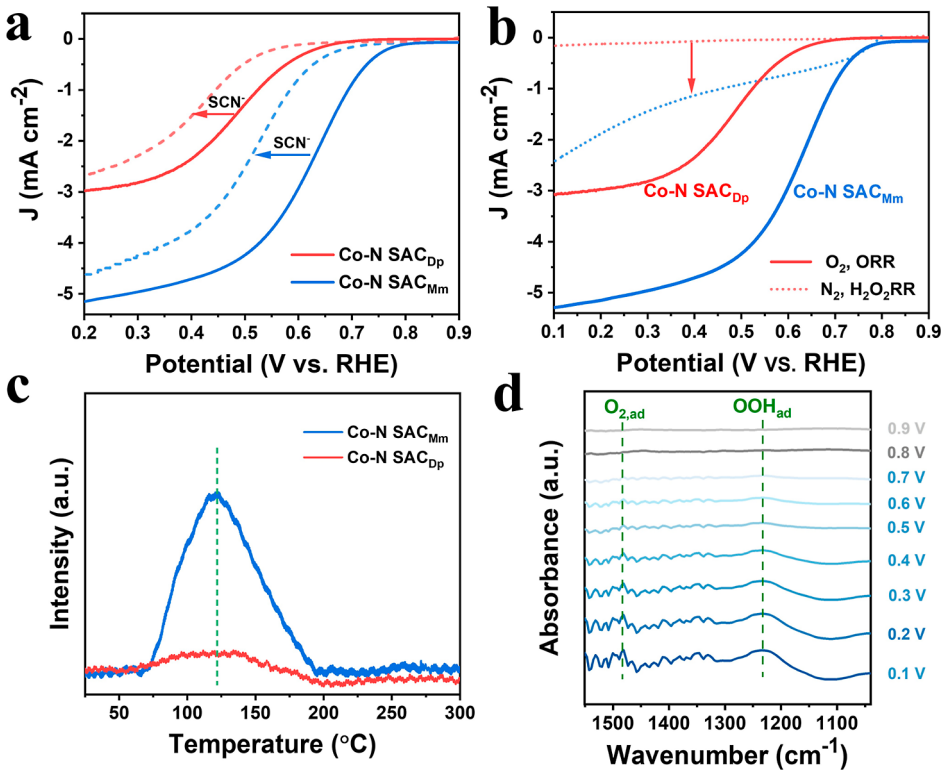

Figure 5. (a) ORR polarization curves in 0.1 M $HClO_4$ before and after the addition of 1 mM SCN^-. (b) ORR polarization curves in 0.1 M $HClO_4$ and H_2O_2RR polarization curves in 0.1 M $HClO_4$ containing 10 mM H_2O_2. (c) O_2-TPD curves for the Co−N SAC_{Dp} and Co−N SAC_{Mm}. (d) *In situ* ATR−SEIRAS spectra for the Co−N SAC_{Dp} at potential range of 0.9−0.1 V.

SAC_{Dp} excels most reported non-noble metal catalysts and is even comparable to advanced noble metal catalysts in acidic media (Figure 4d). These outstanding $2e^-$ ORR performances make the Co−N SAC_{Dp} rank as one of the top catalysts for H_2O_2 production in acidic media (Table S11). It is shown in Figure 4e that the chronoamperometry measurement is performed to assess the catalytic stability of the Co−N SAC_{Dp} on RRDE. The Co−N SAC_{Dp} shows almost unchanged current signals and maintained H_2O_2 selectivity of >90% for 20,000 s, verifying its robust catalytic durability for $2e^-$ ORR in acidic media. The ORR performances of the three Co−N SACs also have been evaluated in the different electrolytes. As displayed in Figures S29 and S30, the ORR activity shows a similar trend to that in acidic media, that is, Co−N SAC_{Mm} > Co−N SAC_{Pc} > Co−N SAC_{Dp}. Also, the Co−N SAC_{Dp} exhibits a higher H_2O_2 selectivity than that of the Co−N SAC_{Pc} and Co−N SAC_{Mm} both in 0.1 M KOH and 0.1 M phosphate-buffered saline (PBS). Especially, the Co−N SAC_{Dp} possesses the maximal H_2O_2 selectivity of 86.1% in 0.1 M KOH (pH = 13) and 88.5% in 0.1 M PBS (pH = 7.2), respectively, demonstrating its greatly promising potential for H_2O_2 production in different environments.

Next, we perform further experimental investigations on the typical $4e^-$ ORR catalyst of the Co−N SAC_{Mm} and $2e^-$ ORR catalyst of the Co−N SAC_{Dp} to probe the origin of different ORR pathways. The SCN^- poisoning experiments (Figure 5a) verify that the Co metal center is the actual active site in the two Co−N SAC. Furthermore, the prepared nitrogen-doped carbon (CN) catalyst without adding Co exhibits much inferior $2e^-$ ORR activity to the Co−N SAC_{Dp} (Figure S31), further confirming the substantial ORR contribution of the Co center. In the N_2-saturated 0.1 M $HClO_4$ containing 10 mM H_2O_2, Co−N SAC_{Dp} shows negligible H_2O_2 reduction reaction (H_2O_2RR) activity while the Co−N SAC_{Mm} exhibits apparent H_2O_2RR current (Figure 5b). That is to say, when the $2e^-$ ORR proceeds, the generated H_2O_2 will be maintained on Co−N SAC_{Dp} resulting in high H_2O_2 selectivity. However, the generated H_2O_2 on Co−N SAC_{Mm} will be reduced to H_2O leading to the dominated $4e^-$ ORR. The O_2 temperature-programed desorption (O_2-TPD) curves show that the Co−N SAC_{Mm} exhibits stronger O_2 adsorption than that of Co−N SAC_{Dp} (Figure 5c), which is in line with the facile O_2 adsorption and activation for pyridine-type CoN_4 (Co−N SAC_{Mm}) in DFT calculation. However, the strong O_2 adsorption for the Co−N SAC_{Mm} will hamper the desorption of HOO* intermediates resulting in $4e^-$ ORR and lowered H_2O_2 selectivity. However, the weak O_2 adsorption may favor the facile HOO* desorption and ensure the high H_2O_2 selectivity for the Co−N SAC_{Dp}. Furthermore, the *in situ* attenuated total reflectance surface−enhanced infrared absorption spectroscopy (ATR−SEIRAS) measurements are performed to detect the reaction intermediate (Figure S32). As shown in Figure 5d, there emerge two absorbance peaks at 1482 and 1231 cm^{-1} which can be attributed to the adsorption of O_2 ($O_{2,ad}$) and HOO* (OOH_{ad}), respectively, according to previous reports.[34,61] A similar OOH_{ad} peak with increasing strength can be observed for Co−N SAC_{Mm} (Figure S33) relative to Co−N SAC_{Dp}. The relatively strong OOH_{ad} peak on the Co−N SAC_{Mm} may be related to the higher coverage of HOO* considering the similar measurement procedure of *in situ* ATR−SEIRAS.[62−64] Summarizing the abovementioned results, we use the experimental evidence to verify the DFT calculation results that the Co−N SAC_{Dp} with pyrrole-type

https://doi.org/10.1021/jacs.2c01194
J. Am. Chem. Soc. 2022, 144, 14505−14516

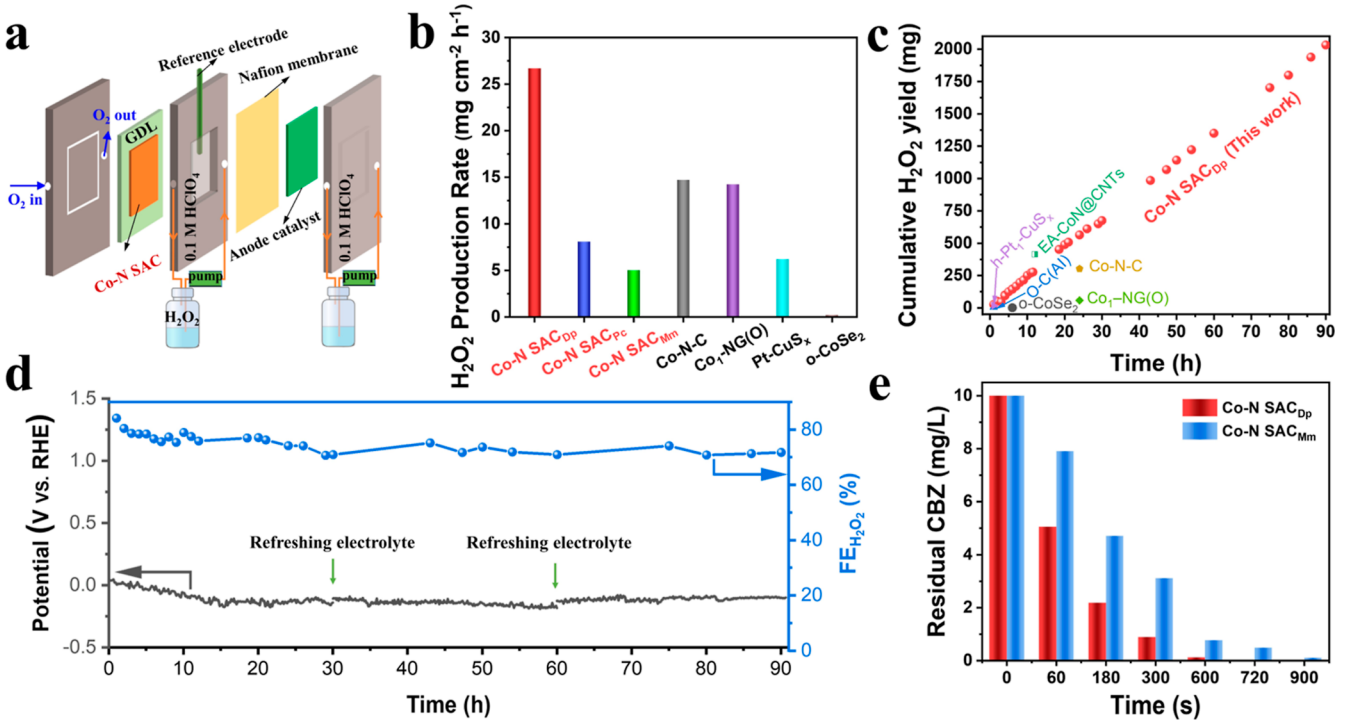

Figure 6. (a) Schematic diagram of the flow cell for H_2O_2 production. (b) H_2O_2 production rate for different catalysts (the catalysts in this work are highlighted in red color and the other catalysts referred to the previous reports in Table S11). (c) Accumulatively produced H_2O_2 for Co−N SAC_{Dp} and previously reported catalysts (detailed information in Table S11). (d) Chronopotentiometry curve at the fixed current of −50 mA and the corresponding $FE_{H_2O_2}$ in the flow cell for Co−N SAC_{Dp}. (e) Residual CBZ concentration at a different time in the electro-Fenton process.

CoN_4 favors the H_2O_2 production as compared to the Co−N SAC_{Mm} (pyridine-type CoN_4).

Furthermore, based on the control experiment and DFT calculation results (Figures S34−S36), we deduce that the oxygen functional groups cannot account for the totally different ORR selectivity for the three Co−N SAC samples and have negligible influence on the H_2O_2 selectivity in the present pyrrole-type CoN_4 system. Noting that the previously reported Co SAC[4,24,34] usually used pyridine-type CoN_4 as the theoretical model and the introduction of the C−O−C group in pyridine-type CoN_4 could enhance the H_2O_2 selectivity. However, according to the theoretical results (Figure S34), the pyrrole-type CoN_4 initially shows high H_2O_2 selectivity, and introducing C−O−C results in lower H_2O_2 selectivity.

H_2O_2 Production Ability and Electro-Fenton Application. Inspired by the outstanding $2e^-$ ORR performances, the H_2O_2 production ability in the amplifying device of the flow cell has been assessed in 0.1 M $HClO_4$. As shown in Figures 6a and S37, the Co−N SAC catalysts have been assembled into the cathode for ORR. Moreover, the IrO_2 coating on the titanium sheet is used as the anode for oxygen evolution reaction, which is separated by the Nafion membrane. The Co−N SAC_{Dp} in the flow cell can reach a large ORR current of −75 mA (Figure S38). As shown in Figure 6b, the Co−N SAC_{Dp} shows a superior H_2O_2 production rate (26.7 mg cm^{-2} h^{-1}) to the Co−N SAC_{Pc} (8.1 mg cm^{-2} h^{-1}) and Co−N SAC_{Mm} (5.0 mg cm^{-2} h^{-1}), consistent with the $2e^-$ ORR activity order on RRDE. Impressively, the H_2O_2 production rate of Co−N SAC_{Dp} surpasses most previously reported catalysts (Figure 6b and Table S11). Furthermore, the longstanding and stable H_2O_2 production has been performed at a fixed current of −50 mA, and the generated H_2O_2 is determined by the Ce^{4+} titration method (Figure S39). It is shown in Figure 6d that the Co−N SAC_{Dp} shows a high $FE_{H_2O_2}$ of 84% in the initial 1 h and maintains the $FE_{H_2O_2}$ of >70% in the continuous H_2O_2 production operation up to 90 h (the electrolyte is periodically refreshed every 30 h). Importantly, the produced H_2O_2 amount linearly increases with the operating time and the cumulative H_2O_2 yield reaches up to 2032 mg for 90 h (Figure 6c), which is one of the highest H_2O_2 production yields in acidic media, to the best of our knowledge (Table S11). Moreover, the Co−N SAC_{Dp} after the stability test shows no aggregated Co nanoparticles and maintains the atomical dispersion of Co species according to the XRD analysis (Figure S40), TEM, and AC-HAADF-STEM results (Figure S41), confirming its robust stability.

In a preliminary application, the collected electrolyte after 30 h is used to decompose 200 ppm of methylene blue (MB, pH = 1, containing 10 mmol Fe^{2+}). After adding the electrolyte to the MB solution, the MB can be totally removed (Figure S42), indicative of the promising potential for pollutant degradation. Furthermore, we also have compared the electro-Fenton activity of the Co−N SAC_{Dp} and Co−N SAC_{Mm}, and the recalcitrant CBZ is selected as the targeted organic pollutant[65] (Figures S43 and S44). As shown in Figure 6e, the Co−N SAC_{Dp} shows a superior degradation ability to the Co−N SAC_{Mm} in which the 10 ppm CBZ can be completely removed within 12 min (Figure S45). Therefore, the remarkable H_2O_2 productivity and outstanding degradation ability make the Co−N SAC_{Dp} a promising and ready catalyst for the actual application.

CONCLUSIONS

In summary, by combining DFT calculations and experiments, we addressed key issues about the structure−function

https://doi.org/10.1021/jacs.2c01194
J. Am. Chem. Soc. 2022, 144, 14505−14516

relationship for a series of Co−N_4 catalysts with different coordination structures and the ORR pathway over this family of SACs. We disclose that the pyrrole-type CoN_4 mainly accounts for the 2e$^-$ ORR for producing H_2O_2, while the pyridine-motif promotes the 4e$^-$ ORR. This striking difference may originate from the electron interaction with the important HOO* intermediate and the accompanying spin state difference between the different coordinations of the active center. Experimentally, a series of Co−N SAC catalysts with different coordination structures were prepared. The Co−N SAC_{Dp} with pyrrole-type of CoN_4 and the Co−N SAC_{Mm} with pyridine-type of CoN_4 showed selectivity toward 2e$^-$ ORR and 4e$^-$ ORR, respectively. Impressively, the Co−N SAC_{Dp} exhibits superior 2e$^-$ ORR performances than most previously reported catalysts in acidic media, with a mass activity of 14.4 A $g_{cat.}^{-1}$ at 0.5 V *versus* RHE and H_2O_2 selectivity of 94% at 0.3 V *versus* RHE. Our experimental results indicate that the Co−N SAC_{Dp} (pyrrole-type CoN_4) with weaker intermediate interaction favors the H_2O_2 production compared to the Co−N SAC_{Mm} (pyridine-type CoN_4). This is also in agreement with our DFT calculation results over these intermediates. Importantly, the Co−N SAC_{Dp} has been tested in a flow cell, accumulating a H_2O_2 yield of 2032 mg for 90 h. As such, this work identifies the pyrrole-type CoN_4 as the highly active Co−N coordination motif for electrosynthesis of H_2O_2, and provides fundamental insights into the ORR mechanism on SAC catalysts and beyond.

■ ASSOCIATED CONTENT

Supporting Information

The Supporting Information is available free of charge at https://pubs.acs.org/doi/10.1021/jacs.2c01194.

Catalyst synthesis, characterization, ORR measurement, kinetic barrier, DOS analysis, SEM images, TEM images, XRD patterns, FT-IR spectra, XANES spectra, O 1s XPS spectra, additional X-ray absorption spectroscopy (XAS) fitting data, N_2 adsorption/desorption isotherms and BET data, ECSA data, additional ORR performance data, *in situ* ATR−SEIRAS setup and spectra, catalyst characterization after stability test, CBZ degradation data, and performance comparison with the reported catalysts (PDF)

■ AUTHOR INFORMATION

Corresponding Authors

Mingshan Zhu − *Guangdong Key Laboratory of Environmental Pollution and Health, School of Environment, Jinan University, 511443 Guangzhou, China*; Email: zhumingshan@jnu.edu.cn

Emiliano Cortés − *Nanoinstitut München, Fakultät für Physik, Ludwig-Maximilians-Universität München, 80539 München, Germany*; orcid.org/0000-0001-8248-4165; Email: emiliano.cortes@lmu.de

Min Liu − *Hunan Joint International Research Center for Carbon Dioxide Resource Utilization, State Key Laboratory of Powder Metallurgy, School of Physical and Electronics, Central South University, 410083 Changsha, China*; orcid.org/0000-0002-9007-4817; Email: minliu@csu.edu.cn

Authors

Shanyong Chen − *Hunan Joint International Research Center for Carbon Dioxide Resource Utilization, State Key Laboratory of Powder Metallurgy, School of Physical and Electronics, Central South University, 410083 Changsha, China; Guangdong Key Laboratory of Environmental Pollution and Health, School of Environment, Jinan University, 511443 Guangzhou, China*; orcid.org/0000-0002-3944-1810

Tao Luo − *Hunan Joint International Research Center for Carbon Dioxide Resource Utilization, State Key Laboratory of Powder Metallurgy, School of Physical and Electronics, Central South University, 410083 Changsha, China*

Xiaoqing Li − *Hunan Joint International Research Center for Carbon Dioxide Resource Utilization, State Key Laboratory of Powder Metallurgy, School of Physical and Electronics, Central South University, 410083 Changsha, China*

Kejun Chen − *Hunan Joint International Research Center for Carbon Dioxide Resource Utilization, State Key Laboratory of Powder Metallurgy, School of Physical and Electronics, Central South University, 410083 Changsha, China*

Junwei Fu − *Hunan Joint International Research Center for Carbon Dioxide Resource Utilization, State Key Laboratory of Powder Metallurgy, School of Physical and Electronics, Central South University, 410083 Changsha, China*; orcid.org/0000-0003-0190-1663

Kang Liu − *Hunan Joint International Research Center for Carbon Dioxide Resource Utilization, State Key Laboratory of Powder Metallurgy, School of Physical and Electronics, Central South University, 410083 Changsha, China*; orcid.org/0000-0002-8781-7747

Chao Cai − *Hunan Joint International Research Center for Carbon Dioxide Resource Utilization, State Key Laboratory of Powder Metallurgy, School of Physical and Electronics, Central South University, 410083 Changsha, China*; orcid.org/0000-0002-3695-3247

Qiyou Wang − *Hunan Joint International Research Center for Carbon Dioxide Resource Utilization, State Key Laboratory of Powder Metallurgy, School of Physical and Electronics, Central South University, 410083 Changsha, China*

Hongmei Li − *Hunan Joint International Research Center for Carbon Dioxide Resource Utilization, State Key Laboratory of Powder Metallurgy, School of Physical and Electronics, Central South University, 410083 Changsha, China*

Yu Chen − *Hunan Joint International Research Center for Carbon Dioxide Resource Utilization, State Key Laboratory of Powder Metallurgy, School of Physical and Electronics, Central South University, 410083 Changsha, China*

Chao Ma − *School of Materials Science and Engineering, Hunan University, Changsha 410082, China*; orcid.org/0000-0001-8599-9340

Li Zhu − *Nanoinstitut München, Fakultät für Physik, Ludwig-Maximilians-Universität München, 80539 München, Germany*

Ying-Rui Lu − *National Synchrotron Radiation Research Center, Hsinchu 30076, Taiwan*; orcid.org/0000-0002-6002-5627

Ting-Shan Chan − *National Synchrotron Radiation Research Center, Hsinchu 30076, Taiwan*

Complete contact information is available at: https://pubs.acs.org/10.1021/jacs.2c01194

Author Contributions

[#]S.C. and T.L. contributed equally.

Notes

The authors declare no competing financial interest.

■ ACKNOWLEDGMENTS

This study was financially supported by the Natural Science Foundation of China (grant nos. 21872174, 22002189, and U1932148), International Science and Technology Cooperation Program (grant no. 2017YFE0127800), China Postdoctoral Science Foundation (2021M701415 and 2022T150265), Hunan Provincial key research and development program (2020WK2002), the Hunan Provincial Natural Science Foundation of China (2020JJ2041 and 2020JJ5691), Hunan Provincial Science and Technology Program (2017XK2026), Guangdong Basic and Applied Basic Research Foundation (nos. 2020B1515020038 and 2021A1515110907), Shenzhen Science and Technology Innovation Project (grant no. JCYJ20180307151313532), Deutsche Forschungsgemeinschaft (DFG, German Research Foundation) under Germany's Excellence Strategy—EXC 2089/1-390776260, the Bavarian program Solar Energies Go Hybrid (SolTech), the Center for NanoScience (CeNS), and the European Commission through the ERC Starting Grant CATALIGHT (802989). M.Z. acknowledges the support of the Pearl River Talent Recruitment Program of Guangdong Province (2019QN01L148). The authors gratefully thank the National Synchrotron Radiation Research Center (NSRRC, the TLS 01C1 and TLS 16A1 beamlines, Taiwan) for XAFS measurement and BL10B in NSRL for soft XAS characterizations by Synchrotron Radiation. We are grateful for resources from the High Performance Computing Center of Central South University.

■ REFERENCES

(1) Xia, C.; Xia, Y.; Zhu, P.; Fan, L.; Wang, H. Direct electrosynthesis of pure aqueous H_2O_2 solutions up to 20% by weight using a solid electrolyte. *Science* **2019**, *366*, 226−231.

(2) Bu, Y.; Wang, Y.; Han, G.-F.; Zhao, Y.; Ge, X.; Li, F.; Zhang, Z.; Zhong, Q.; Baek, J.-B. Carbon-Based Electrocatalysts for Efficient Hydrogen Peroxide Production. *Adv. Mater.* **2021**, *33*, 2103266.

(3) Jiang, K.; Back, S.; Akey, A. J.; Xia, C.; Hu, Y.; Liang, W.; Schaak, D.; Stavitski, E.; Nørskov, J. K.; Siahrostami, S.; Wang, H. Highly selective oxygen reduction to hydrogen peroxide on transition metal single atom coordination. *Nat. Commun.* **2019**, *10*, 3997.

(4) Jung, E.; Shin, H.; Lee, B.-H.; Efremov, V.; Lee, S.; Lee, H. S.; Kim, J.; Hooch Antink, W.; Park, S.; Lee, K.-S.; Cho, S.-P.; Yoo, J. S.; Sung, Y.-E.; Hyeon, T. Atomic-level tuning of Co−N−C catalyst for high-performance electrochemical H_2O_2 production. *Nat. Mater.* **2020**, *19*, 436−442.

(5) Gao, R.; Pan, L.; Li, Z.; Shi, C.; Yao, Y.; Zhang, X.; Zou, J.-J. Engineering Facets and Oxygen Vacancies over Hematite Single Crystal for Intensified Electrocatalytic H_2O_2 Production. *Adv. Funct. Mater.* **2020**, *30*, 1910539.

(6) Li, B.-Q.; Zhao, C.-X.; Liu, J.-N.; Zhang, Q. Electrosynthesis of Hydrogen Peroxide Synergistically Catalyzed by Atomic Co−N_x−C Sites and Oxygen Functional Groups in Noble-Metal-Free Electrocatalysts. *Adv. Mater.* **2019**, *31*, 1808173.

(7) Jia, Y.; Xue, Z.; Yang, J.; Liu, Q.; Xian, J.; Zhong, Y.; Sun, Y.; Zhang, X.; Liu, Q.; Yao, D.; Li, G. Tailoring the Electronic Structure of an Atomically Dispersed Zinc Electrocatalyst: Coordination Environment Regulation for High Selectivity Oxygen Reduction. *Angew. Chem., Int. Ed.* **2022**, *61*, No. e202110838.

(8) Choi, C. H.; Kim, M.; Kwon, H. C.; Cho, S. J.; Yun, S.; Kim, H.-T.; Mayrhofer, K. J. J.; Kim, H.; Choi, M. Tuning selectivity of electrochemical reactions by atomically dispersed platinum catalyst. *Nat. Commun.* **2016**, *7*, 10922.

(9) Xia, F.; Li, B.; Liu, Y.; Liu, Y.; Gao, S.; Lu, K.; Kaelin, J.; Wang, R.; Marks, T. J.; Cheng, Y. Carbon Free and Noble Metal Free $Ni_2Mo_6S_8$ Electrocatalyst for Selective Electrosynthesis of H_2O_2. *Adv. Funct. Mater.* **2021**, *31*, 2104716.

(10) Wang, Y.; Shi, R.; Shang, L.; Waterhouse, G. I. N.; Zhao, J.; Zhang, Q.; Gu, L.; Zhang, T. High-Efficiency Oxygen Reduction to Hydrogen Peroxide Catalyzed by Nickel Single-Atom Catalysts with Tetradentate N_2O_2 Coordination in a Three-Phase Flow Cell. *Angew. Chem., Int. Ed.* **2020**, *59*, 13057−13062.

(11) Liu, W.; Feng, J.; Yin, R.; Ni, Y.; Zheng, D.; Que, W.; Niu, X.; Dai, X.; Shi, W.; Wu, F.; Yang, J.; Cao, X. Tailoring oxygenated groups of monolithic cobalt-nitrogen-carbon frameworks for highly efficient hydrogen peroxide production in acidic media. *Chem. Eng. J.* **2022**, *430*, 132990.

(12) Tang, C.; Jiao, Y.; Shi, B.; Liu, J.-N.; Xie, Z.; Chen, X.; Zhang, Q.; Qiao, S.-Z. Coordination Tunes Selectivity: Two-Electron Oxygen Reduction on High-Loading Molybdenum Single-Atom Catalysts. *Angew. Chem., Int. Ed.* **2020**, *59*, 9171−9176.

(13) Li, L.; Tang, C.; Zheng, Y.; Xia, B.; Zhou, X.; Xu, H.; Qiao, S.-Z. Tailoring Selectivity of Electrochemical Hydrogen Peroxide Generation by Tunable Pyrrolic-Nitrogen-Carbon. *Adv. Energy Mater.* **2020**, *10*, 2000789.

(14) Dong, K.; Lei, Y.; Zhao, H.; Liang, J.; Ding, P.; Liu, Q.; Xu, Z.; Lu, S.; Li, Q.; Sun, X. Noble-metal-free electrocatalysts toward H_2O_2 production. *J. Mater. Chem. A* **2020**, *8*, 23123−23141.

(15) Wang, Y.; Waterhouse, G. I. N.; Shang, L.; Zhang, T. Electrocatalytic Oxygen Reduction to Hydrogen Peroxide: From Homogeneous to Heterogeneous Electrocatalysis. *Adv. Energy Mater.* **2021**, *11*, 2003323.

(16) Wang, M.; Zhang, N.; Feng, Y.; Hu, Z.; Shao, Q.; Huang, X. Partially Pyrolyzed Binary Metal-Organic Framework Nanosheets for Efficient Electrochemical Hydrogen Peroxide Synthesis. *Angew. Chem., Int. Ed.* **2020**, *59*, 14373−14377.

(17) Chen, S.; Luo, T.; Chen, K.; Lin, Y.; Fu, J.; Liu, K.; Cai, C.; Wang, Q.; Li, H.; Li, X.; Hu, J.; Li, H.; Zhu, M.; Liu, M. Chemical Identification of Catalytically Active Sites on Oxygen-doped Carbon Nanosheet to Decipher the High Activity for Electro-synthesis Hydrogen Peroxide. *Angew. Chem., Int. Ed.* **2021**, *60*, 16607−16614.

(18) Yang, Q.; Xu, W.; Gong, S.; Zheng, G.; Tian, Z.; Wen, Y.; Peng, L.; Zhang, L.; Lu, Z.; Chen, L. Atomically dispersed Lewis acid sites boost 2-electron oxygen reduction activity of carbon-based catalysts. *Nat. Commun.* **2020**, *11*, 5478.

(19) Xu, Z.; Liang, J.; Wang, Y.; Dong, K.; Shi, X.; Liu, Q.; Luo, Y.; Li, T.; Jia, Y.; Asiri, A. M.; Feng, Z.; Wang, Y.; Ma, D.; Sun, X. Enhanced Electrochemical H_2O_2 Production via Two-Electron Oxygen Reduction Enabled by Surface-Derived Amorphous Oxygen-Deficient TiO_{2-x}. *ACS Appl. Mater. Interfaces* **2021**, *13*, 33182−33187.

(20) Zhang, F.; Zhu, Y.; Tang, C.; Chen, Y.; Qian, B.; Hu, Z.; Chang, Y.-C.; Pao, C.-W.; Lin, Q.; Kazemi, S. A.; Wang, Y.; Zhang, L.; Zhang, X.; Wang, H. High-Efficiency Electrosynthesis of Hydrogen Peroxide from Oxygen Reduction Enabled by a Tungsten Single Atom Catalyst with Unique Terdentate N_1O_2 Coordination. *Adv. Funct. Mater.* **2021**, *32*, 2110224.

(21) Xia, Y.; Zhao, X.; Xia, C.; Wu, Z.-Y.; Zhu, P.; Kim, J. Y.; Bai, X.; Gao, G.; Hu, Y.; Zhong, J.; Liu, Y.; Wang, H. Highly active and selective oxygen reduction to H_2O_2 on boron-doped carbon for high production rates. *Nat. Commun.* **2021**, *12*, 4225.

(22) Zhang, X.; Xia, Y.; Xia, C.; Wang, H. Insights into Practical-Scale Electrochemical H_2O_2 Synthesis. *Trends Chem.* **2020**, *2*, 942−953.

(23) Chang, Q.; Zhang, P.; Mostaghimi, A. H. B.; Zhao, X.; Denny, S. R.; Lee, J. H.; Gao, H.; Zhang, Y.; Xin, H. L.; Siahrostami, S.; Chen, J. G.; Chen, Z. Promoting H_2O_2 production via 2-electron oxygen reduction by coordinating partially oxidized Pd with defect carbon. *Nat. Commun.* **2020**, *11*, 2178.

(24) Zhang, Q.; Tan, X.; Bedford, N. M.; Han, Z.; Thomsen, L.; Smith, S.; Amal, R.; Lu, X. Direct insights into the role of epoxy groups on cobalt sites for acidic H_2O_2 production. *Nat. Commun.* **2020**, *11*, 4181.
(25) Siahrostami, S.; Verdaguer-Casadevall, A.; Karamad, M.; Deiana, D.; Malacrida, P.; Wickman, B.; Escudero-Escribano, M.; Paoli, E. A.; Frydendal, R.; Hansen, T. W.; Chorkendorff, I.; Stephens, I. E. L.; Rossmeisl, J. Enabling direct H_2O_2 production through rational electrocatalyst design. *Nat. Mater.* **2013**, *12*, 1137−1143.
(26) Verdaguer-Casadevall, A.; Deiana, D.; Karamad, M.; Siahrostami, S.; Malacrida, P.; Hansen, T. W.; Rossmeisl, J.; Chorkendorff, I.; Stephens, I. E. L. Trends in the Electrochemical Synthesis of H_2O_2: Enhancing Activity and Selectivity by Electrocatalytic Site Engineering. *Nano Lett.* **2014**, *14*, 1603−1608.
(27) Fortunato, G. V.; Pizzutilo, E.; Mingers, A. M.; Kasian, O.; Cherevko, S.; Cardoso, E. S. F.; Mayrhofer, K. J. J.; Maia, G.; Ledendecker, M. Impact of Palladium Loading and Interparticle Distance on the Selectivity for the Oxygen Reduction Reaction toward Hydrogen Peroxide. *J. Phys. Chem. C* **2018**, *122*, 15878−15885.
(28) Jirkovský, J. S.; Halasa, M.; Schiffrin, D. J. Kinetics of electrocatalytic reduction of oxygen and hydrogen peroxide on dispersed gold nanoparticles. *Phys. Chem. Chem. Phys.* **2010**, *12*, 8042−8053.
(29) Sheng, H.; Janes, A. N.; Ross, R. D.; Kaiman, D.; Huang, J.; Song, B.; Schmidt, J. R.; Jin, S. Stable and selective electrosynthesis of hydrogen peroxide and the electro-Fenton process on $CoSe_2$ polymorph catalysts. *Energy Environ. Sci.* **2020**, *13*, 4189−4203.
(30) Sheng, H.; Hermes, E. D.; Yang, X.; Ying, D.; Janes, A. N.; Li, W.; Schmidt, J. R.; Jin, S. Electrocatalytic Production of H_2O_2 by Selective Oxygen Reduction Using Earth-Abundant Cobalt Pyrite (CoS_2). *ACS Catal.* **2019**, *9*, 8433−8442.
(31) Zhang, X.-L.; Su, X.; Zheng, Y.-R.; Hu, S.-J.; Shi, L.; Gao, F.-Y.; Yang, P.-P.; Niu, Z.-Z.; Wu, Z.-Z.; Qin, S.; Wu, R.; Duan, Y.; Gu, C.; Zheng, X.-S.; Zhu, J.-F.; Gao, M.-R. Strongly Coupled Cobalt Diselenide Monolayers for Selective Electrocatalytic Oxygen Reduction to H_2O_2 under Acidic Conditions. *Angew. Chem., Int. Ed.* **2021**, *60*, 26922−26931.
(32) Liang, J.; Wang, Y.; Liu, Q.; Luo, Y.; Li, T.; Zhao, H.; Lu, S.; Zhang, F.; Asiri, A. M.; Liu, F.; Ma, D.; Sun, X. Electrocatalytic hydrogen peroxide production in acidic media enabled by NiS_2 nanosheets. *J. Mater. Chem. A* **2021**, *9*, 6117−6122.
(33) Ross, R. D.; Sheng, H.; Parihar, A.; Huang, J.; Jin, S. Compositionally Tuned Trimetallic Thiospinel Catalysts for Enhanced Electrosynthesis of Hydrogen Peroxide and Built-In Hydroxyl Radical Generation. *ACS Catal.* **2021**, *11*, 12643−12650.
(34) Tang, C.; Chen, L.; Li, H.; Li, L.; Jiao, Y.; Zheng, Y.; Xu, H.; Davey, K.; Qiao, S.-Z. Tailoring Acidic Oxygen Reduction Selectivity on Single-Atom Catalysts via Modification of First and Second Coordination Spheres. *J. Am. Chem. Soc.* **2021**, *143*, 7819−7827.
(35) Zhao, Q.; Wang, Y.; Lai, W.-H.; Xiao, F.; Lyu, Y.; Liao, C.; Shao, M. Approaching a high-rate and sustainable production of hydrogen peroxide: oxygen reduction on Co-N-C single-atom electrocatalysts in simulated seawater. *Energy Environ. Sci.* **2021**, *14*, 5444−5456.
(36) Shen, R.; Chen, W.; Peng, Q.; Lu, S.; Zheng, L.; Cao, X.; Wang, Y.; Zhu, W.; Zhang, J.; Zhuang, Z.; Chen, C.; Wang, D.; Li, Y. High-Concentration Single Atomic Pt Sites on Hollow CuSx for Selective O_2 Reduction to H_2O_2 in Acid Solution. *Chem* **2019**, *5*, 2099−2110.
(37) Gao, J.; Liu, B. Progress of Electrochemical Hydrogen Peroxide Synthesis over Single Atom Catalysts. *ACS Mater. Lett.* **2020**, *2*, 1008−1024.
(38) Zhu, Y.; Li, J.; Chen, Y.; Zou, J.; Cheng, Q.; Chen, C.; Hu, W.; Zou, L.; Zou, Z.; Yang, B.; Yang, H. Switching the Oxygen Reduction Reaction Pathway via Tailoring the Electronic Structure of FeN_4/C Catalysts. *ACS Catal.* **2021**, *11*, 13020−13027.
(39) Park, J.; Nabae, Y.; Hayakawa, T.; Kakimoto, M.-a. Highly Selective Two-Electron Oxygen Reduction Catalyzed by Mesoporous Nitrogen-Doped Carbon. *ACS Catal.* **2014**, *4*, 3749−3754.
(40) Pang, Y.; Wang, K.; Xie, H.; Sun, Y.; Titirici, M.-M.; Chai, G.-L. Mesoporous Carbon Hollow Spheres as Efficient Electrocatalysts for Oxygen Reduction to Hydrogen Peroxide in Neutral Electrolytes. *ACS Catal.* **2020**, *10*, 7434−7442.
(41) Iglesias, D.; Giuliani, A.; Melchionna, M.; Marchesan, S.; Criado, A.; Nasi, L.; Bevilacqua, M.; Tavagnacco, C.; Vizza, F.; Prato, M.; Fornasiero, P. N-Doped Graphitized Carbon Nanohorns as a Forefront Electrocatalyst in Highly Selective O_2 Reduction to H_2O_2. *Chem* **2018**, *4*, 106−123.
(42) Gao, J.; Yang, H. b.; Huang, X.; Hung, S.-F.; Cai, W.; Jia, C.; Miao, S.; Chen, H. M.; Yang, X.; Huang, Y.; Zhang, T.; Liu, B. Enabling Direct H_2O_2 Production in Acidic Media through Rational Design of Transition Metal Single Atom Catalyst. *Chem* **2020**, *6*, 658−674.
(43) Sun, Y.; Silvioli, L.; Sahraie, N. R.; Ju, W.; Li, J.; Zitolo, A.; Li, S.; Bagger, A.; Arnarson, L.; Wang, X.; Moeller, T.; Bernsmeier, D.; Rossmeisl, J.; Jaouen, F.; Strasser, P. Activity-Selectivity Trends in the Electrochemical Production of Hydrogen Peroxide over Single-Site Metal-Nitrogen-Carbon Catalysts. *J. Am. Chem. Soc.* **2019**, *141*, 12372−12381.
(44) Wu, F.; Pan, C.; He, C.-T.; Han, Y.; Ma, W.; Wei, H.; Ji, W.; Chen, W.; Mao, J.; Yu, P.; Wang, D.; Mao, L.; Li, Y. Single-Atom Co−N_4 Electrocatalyst Enabling Four-Electron Oxygen Reduction with Enhanced Hydrogen Peroxide Tolerance for Selective Sensing. *J. Am. Chem. Soc.* **2020**, *142*, 16861−16867.
(45) Han, Y.; Wang, Y.-G.; Chen, W.; Xu, R.; Zheng, L.; Zhang, J.; Luo, J.; Shen, R.-A.; Zhu, Y.; Cheong, W.-C.; Chen, C.; Peng, Q.; Wang, D.; Li, Y. Hollow N-Doped Carbon Spheres with Isolated Cobalt Single Atomic Sites: Superior Electrocatalysts for Oxygen Reduction. *J. Am. Chem. Soc.* **2017**, *139*, 17269−17272.
(46) He, Y.; Shi, Q.; Shan, W.; Li, X.; Kropf, A. J.; Wegener, E. C.; Wright, J.; Karakalos, S.; Su, D.; Cullen, D. A.; Wang, G.; Myers, D. J.; Wu, G. Dynamically Unveiling Metal−Nitrogen Coordination during Thermal Activation to Design High-Efficient Atomically Dispersed CoN_4 Active Sites. *Angew. Chem., Int. Ed.* **2021**, *60*, 9516−9526.
(47) Wang, X. X.; Cullen, D. A.; Pan, Y.-T.; Hwang, S.; Wang, M.; Feng, Z.; Wang, J.; Engelhard, M. H.; Zhang, H.; He, Y.; Shao, Y.; Su, D.; More, K. L.; Spendelow, J. S.; Wu, G. Nitrogen-Coordinated Single Cobalt Atom Catalysts for Oxygen Reduction in Proton Exchange Membrane Fuel Cells. *Adv. Mater.* **2018**, *30*, 1706758.
(48) He, Y.; Guo, H.; Hwang, S.; Yang, X.; He, Z.; Braaten, J.; Karakalos, S.; Shan, W.; Wang, M.; Zhou, H.; Feng, Z.; More, K. L.; Wang, G.; Su, D.; Cullen, D. A.; Fei, L.; Litster, S.; Wu, G. Single Cobalt Sites Dispersed in Hierarchically Porous Nanofiber Networks for Durable and High-Power PGM-Free Cathodes in Fuel Cells. *Adv. Mater.* **2020**, *32*, 2003577.
(49) Wu, D.; Hu, J.; Zhu, C.; Zhang, J.; Jing, H.; Hao, C.; Shi, Y. Salt melt synthesis of Chlorella-derived nitrogen-doped porous carbon with atomically dispersed CoN_4 sites for efficient oxygen reduction reaction. *J. Colloid Interface Sci.* **2021**, *586*, 498−504.
(50) Kulkarni, A.; Siahrostami, S.; Patel, A.; Nørskov, J. K. Understanding Catalytic Activity Trends in the Oxygen Reduction Reaction. *Chem. Rev.* **2018**, *118*, 2302−2312.
(51) Duan, Z.; Henkelman, G. Surface Charge and Electrostatic Spin Crossover Effects in CoN_4 Electrocatalysts. *ACS Catal.* **2020**, *10*, 12148−12155.
(52) Chen, Z.; Niu, H.; Ding, J.; Liu, H.; Chen, P.-H.; Lu, Y.-H.; Lu, Y.-R.; Zuo, W.; Han, L.; Guo, Y.; Hung, S.-F.; Zhai, Y. Unraveling the Origin of Sulfur-Doped Fe-N-C Single-Atom Catalyst for Enhanced Oxygen Reduction Activity: Effect of Iron Spin-State Tuning. *Angew. Chem., Int. Ed.* **2021**, *60*, 25404−25410.
(53) Menga, D.; Low, J. L.; Li, Y.-S.; Arčon, I.; Koyutürk, B.; Wagner, F.; Ruiz-Zepeda, F.; Gaberšček, M.; Paulus, B.; Fellinger, T.-P. Resolving the Dilemma of Fe-N-C Catalysts by the Selective Synthesis of Tetrapyrrolic Active Sites via an Imprinting Strategy. *J. Am. Chem. Soc.* **2021**, *143*, 18010−18019.
(54) Wang, H.; Shao, Y.; Mei, S.; Lu, Y.; Zhang, M.; Sun, J.-k.; Matyjaszewski, K.; Antonietti, M.; Yuan, J. Polymer-Derived

Heteroatom-Doped Porous Carbon Materials. *Chem. Rev.* **2020**, *120*, 9363−9419.
(55) Chen, S.; Bi, F.; Xiang, K.; Zhang, Y.; Hao, P.; Li, M.; Zhao, B.; Guo, X. Reactive Template-Derived CoFe/N-Doped Carbon Nanosheets as Highly Efficient Electrocatalysts toward Oxygen Reduction, Oxygen Evolution, and Hydrogen Evolution. *ACS Sustainable Chem. Eng.* **2019**, *7*, 15278−15288.
(56) Chen, S.; Yan, Y.; Hao, P.; Li, M.; Liang, J.; Guo, J.; Zhang, Y.; Chen, S.; Ding, W.; Guo, X. Iron Nanoparticles Encapsulated in S,N-Codoped Carbon: Sulfur Doping Enriches Surface Electron Density and Enhances Electrocatalytic Activity toward Oxygen Reduction. *ACS Appl. Mater. Interfaces* **2020**, *12*, 12686−12695.
(57) Zhang, N.; Zhou, T.; Chen, M.; Feng, H.; Yuan, R.; Zhong, C. a.; Yan, W.; Tian, Y.; Wu, X.; Chu, W.; Wu, C.; Xie, Y. High-purity pyrrole-type FeN_4 sites as a superior oxygen reduction electrocatalyst. *Energy Environ. Sci.* **2020**, *13*, 111−118.
(58) Zhang, Z.; Dou, M.; Ji, J.; Wang, F. Phthalocyanine tethered iron phthalocyanine on graphitized carbon black as superior electrocatalyst for oxygen reduction reaction. *Nano Energy* **2017**, *34*, 338−343.
(59) Lin, Y.; Liu, K.; Chen, K.; Xu, Y.; Li, H.; Hu, J.; Lu, Y.-R.; Chan, T.-S.; Qiu, X.; Fu, J.; Liu, M. Tuning Charge Distribution of FeN_4 via External N for Enhanced Oxygen Reduction Reaction. *ACS Catal.* **2021**, *11*, 6304−6315.
(60) Chen, K.; Liu, K.; An, P.; Li, H.; Lin, Y.; Hu, J.; Jia, C.; Fu, J.; Li, H.; Liu, H.; Lin, Z.; Li, W.; Li, J.; Lu, Y.-R.; Chan, T.-S.; Zhang, N.; Liu, M. Iron phthalocyanine with coordination induced electronic localization to boost oxygen reduction reaction. *Nat. Commun.* **2020**, *11*, 4173.
(61) Nayak, S.; McPherson, I. J.; Vincent, K. A. Adsorbed Intermediates in Oxygen Reduction on Platinum Nanoparticles Observed by In Situ IR Spectroscopy. *Angew. Chem., Int. Ed.* **2018**, *57*, 12855−12858.
(62) Wang, T.; Zhang, Y.; Huang, B.; Cai, B.; Rao, R. R.; Giordano, L.; Sun, S.-G.; Shao-Horn, Y. Enhancing oxygen reduction electrocatalysis by tuning interfacial hydrogen bonds. *Nat. Catal.* **2021**, *4*, 753−762.
(63) Ohta, N.; Nomura, K.; Yagi, I. Adsorption and Electroreduction of Oxygen on Gold in Acidic Media: In Situ Spectroscopic Identification of Adsorbed Molecular Oxygen and Hydrogen Superoxide. *J. Phys. Chem. C* **2012**, *116*, 14390−14400.
(64) Zhou, P.; Li, L.; Mosali, V. S. S.; Chen, Y.; Luan, P.; Gu, Q.; Turner, D. R.; Huang, L.; Zhang, J. Electrochemical Hydrogenation of Furfural in Aqueous Acetic Acid Media with Enhanced 2-Methylfuran Selectivity Using CuPd Bimetallic Catalysts. *Angew. Chem., Int. Ed.* **2022**, *61*, No. e202117809.
(65) Zhang, L.; Zhao, X.; Niu, C.; Tang, N.; Guo, H.; Wen, X.; Liang, C.; Zeng, G. Enhanced activation of peroxymonosulfate by magnetic Co_3MnFeO_6 nanoparticles for removal of carbamazepine: Efficiency, synergetic mechanism and stability. *Chem. Eng. J.* **2019**, *362*, 851−864.

https://doi.org/10.1021/jacs.2c01194
J. Am. Chem. Soc. 2022, 144, 14505−14516